

Plasma Physics and Controlled Fusion

Crossmark

PAPER

RECEIVED

dd Month yyyy

REVISED

dd Month yyyy

A High-order piecewise field-aligned triangular finite element method for electromagnetic gyrokinetic particle simulations of tokamak plasmas with open field lines

Zhixin Lu^{1*}, Guo Meng^{1*}, Eric Sonnendrücker¹, Roman Hatzky¹, Giorgio Daneri¹, Gengxian Li¹, Peiyou Jiang¹, Klaus Reuter², Matthias Hoelzl¹

¹Max Planck Institute for Plasma Physics, Boltzmannstr. 2, Garching, 85748, Germany ²Max Planck Computing and Data Facility, Giessenbachstrasse 2, Garching, 85748, Germany

* Author to whom any correspondence should be addressed (zhixin.lu@ipp.mpg.de; guo.meng@ipp.mpg.de).

Keywords: Whole volume simulations, Electromagnetic gyrokinetic simulation, particle-in-cell, turbulence, Alfvén modes, finite element method, triangular meshes, field-aligned, tokamak, magnetic confinement fusion, divertor tokamak, open field lines

Abstract

A high-order piecewise field-aligned triangular finite element method is developed and implemented for global electromagnetic gyrokinetic particle-in-cell simulations of tokamak plasmas with open field lines. The approach combines locally field-aligned finite element basis functions with unstructured C^1 triangular meshes in cylindrical coordinates, enabling whole-volume simulations with substantially reduced computational effort, while avoiding the grid distortion associated with globally field-aligned coordinates and the associated singularity at the separatrix of diverted plasmas. The formulation is compatible with both δf and full- f models and employs mixed-variable representations, along with a generalized pullback scheme, to control numerical cancellation in electromagnetic simulations. The method is implemented in the TRIMEG-C1 code and demonstrated using linear and nonlinear electromagnetic simulations of the TCV-X21 configuration. The results indicate that the approach accurately captures the key features of electromagnetic ion-temperature-gradient and kinetic ballooning mode physics, including the separatrix regions in the simulation, thereby providing a robust framework for whole-volume electromagnetic gyrokinetic simulations in realistic tokamak geometries.

1 Introduction

Electromagnetic effects are essential for accurately describing microinstabilities and turbulence in magnetically confined fusion plasmas, including ion-temperature-gradient (ITG) modes, kinetic ballooning modes (KBMs), and Alfvénic fluctuations. Their importance increases at finite plasma pressure β , particularly in global simulations that span both core and edge regions. First-principles electromagnetic gyrokinetic simulations are therefore a key tool for predictive modelling of tokamak plasmas [1, 2, 3]. Global gyrokinetic particle-in-cell (PIC) simulations in realistic geometry remain numerically challenging due to strong scale anisotropy (the wave vector component along the magnetic field line is much smaller than the perpendicular component, $k_{\parallel} \ll k_{\perp}$), magnetic shear, and the presence of open magnetic field lines outside the separatrix. While globally field-aligned coordinate systems reduce numerical stiffness along magnetic field lines, they often suffer from severe grid distortion in whole-volume simulations and exhibit a singularity on the separatrix. Finite element methods on unstructured meshes offer greater geometric flexibility [4], especially when combined with high-order basis functions that improve numerical accuracy [5].

To exploit field-line alignment while avoiding global grid distortion, a *piecewise* field-aligned finite element method has been proposed, in which basis functions are locally aligned with magnetic field lines within each toroidal subdomain [6]. It has been originally implemented in the TRIMEG-GKX code for core plasma without open field lines [7]. This approach preserves continuity along field lines and significantly reduces numerical errors associated with parallel dynamics. Similar ideas have been used for Finite Difference schemes. Specifically, the flux-coordinate independent (FCI) approach has previously been developed to improve efficiency and accuracy along the magnetic field [8, 9], and the shifted metric procedure has been developed to reduce the grid distortion [10]. Our scheme is formulated using the finite element method (FEM), thereby inheriting the advantageous features of

FEM, such as its ability to handle complex, curved, and irregular geometries and refinement. Additionally, mixed-variable formulations combined with pullback schemes are essential for controlling numerical cancellation in electromagnetic gyrokinetic PIC simulations [11, 12, 13].

In this work, we extend the piecewise field-aligned finite element method (PFAFEM) to global electromagnetic gyrokinetic simulations with *open* field lines. The PFAFEM enables us to use an identical mesh structure at different toroidal locations, which differs from that in XGC [14]. The formulation is implemented in cylindrical coordinates in the TRIMEG-C1 code using high-order C^1 finite elements on triangular meshes in the poloidal cross section. It is compatible with both δf and full- f models. The method incorporates generalized pullback schemes and an efficient iterative treatment of Ampère's law. Its capabilities are demonstrated through electromagnetic simulations of the TCV configuration, which capture key features of ITG and KBM physics in both the core and near-separatrix regions. The remainder of the paper is organized as follows. Section 2 introduces the gyrokinetic model and electromagnetic field equations. Section 3 describes the piecewise field-aligned finite element formulation and the corresponding field solvers. Simulation setup and numerical results are presented in Section 4, followed by conclusions in Section 5.

2 Models and equations

The mixed variable–pullback scheme has been studied extensively in previous work [11, 12, 2] and was recently generalized to allow for various choices of the evolution equation for the symplectic part of δA_{\parallel} [13]. Two such schemes that are most suitable for TRIMEG-C1 have been implemented in this work, as introduced in the following.

2.1 Physics equations using mixed variables

Using the mixed variable scheme, the parallel component δA_{\parallel} of the perturbed magnetic potential is decomposed into a symplectic part and a Hamiltonian part [11],

$$\delta A_{\parallel} = \delta A_{\parallel}^s + \delta A_{\parallel}^h . \quad (1)$$

The shifted parallel velocity coordinate of the gyrocenter u_{\parallel} is defined as

$$u_{\parallel} = v_{\parallel} + \frac{q_s}{m_s} \langle \delta A_{\parallel}^h \rangle , \quad (2)$$

where v_{\parallel} is the parallel velocity, q_s and m_s are the charge and mass of species s , respectively, the subscript “ s ” represents the different particle species, and $\langle \dots \rangle$ indicates the gyro average.

The gyrocenter equations of motion are consistent with previous work [11, 12, 2, 15, 16],

$$\dot{\mathbf{R}}_0 = u_{\parallel} \mathbf{b}_0^* + \frac{m\mu}{qB_{\parallel}^*} \mathbf{b} \times \nabla B , \quad (3)$$

$$\dot{u}_{\parallel,0} = -\mu \mathbf{b}_0^* \cdot \nabla B , \quad (4)$$

$$\delta \dot{\mathbf{R}} = \frac{\mathbf{b}}{B_{\parallel}^*} \times \nabla \langle \delta \Phi - u_{\parallel} \delta A_{\parallel} \rangle - \frac{q_s}{m_s} \langle \delta A_{\parallel}^h \rangle \mathbf{b}^* , \quad (5)$$

$$\begin{aligned} \delta \dot{u}_{\parallel} = & -\frac{q_s}{m_s} \left(\mathbf{b}^* \cdot \nabla \langle \delta \Phi - u_{\parallel} \delta A_{\parallel} \rangle + \partial_t \langle \delta A_{\parallel}^s \rangle \right) \\ & - \frac{\mu}{B_{\parallel}^*} \mathbf{b} \times \nabla B \cdot \nabla \langle \delta A_{\parallel}^s \rangle , \end{aligned} \quad (6)$$

where the magnetic moment $\mu = v_{\perp}^2/(2B)$, $\mathbf{b}^* = \mathbf{b}_0^* + \nabla \times (\mathbf{b} \langle \delta A_{\parallel}^s \rangle)/B_{\parallel}^* \approx \mathbf{b}_0^* + \nabla \langle \delta A_{\parallel}^s \rangle \times \mathbf{b}/B_{\parallel}^*$, $\mathbf{b}_0^* = \mathbf{b} + (m_s/q_s)u_{\parallel}\nabla \times \mathbf{b}/B_{\parallel}^*$, $\mathbf{b} = \mathbf{B}/B$, \mathbf{B} is the equilibrium magnetic field, $B_{\parallel}^* = B + (m_s/q_s)u_{\parallel}\mathbf{b} \cdot (\nabla \times \mathbf{b})$. In obtaining the approximated form of \mathbf{b}^* , we made use of the following simplification of the perturbed magnetic field $\mathbf{B}_1 = \nabla \times (\delta A_{\parallel} \mathbf{b}) = \nabla \delta A_{\parallel} \times \mathbf{b} + \delta A_{\parallel} \nabla \times \mathbf{b} = \nabla \delta A_{\parallel} \times \mathbf{b} + \delta A_{\parallel} (\mathbf{b} \cdot \boldsymbol{\kappa} + (\mathbf{b} \cdot \nabla \times \mathbf{b})\mathbf{b}) \approx \nabla \delta A_{\parallel} \times \mathbf{b}$ where $\boldsymbol{\kappa} = (\mathbf{b} \cdot \nabla)\mathbf{b}$ is the curvature of the equilibrium magnetic field lines. The modified magnetic field is then $\mathbf{B}^* = \mathbf{B} + \mathbf{B}_1 + (m_s/q_s)u_{\parallel}\nabla \times \mathbf{b}$. Note that $\nabla \cdot \mathbf{B}^*$ is not exactly zero, since $\nabla \cdot \mathbf{B}_1 \neq 0$ due to the approximation. The expression of the gyrocenter equation of motion Eqs. (3)–(6) in (R, ϕ, Z) coordinates used in TRIMEG-C1 is listed in [5].

The distribution function is decomposed into the equilibrium one, and the perturbed one $f = f_0 + \delta f$, and δf is solved along the particle trajectory using the standard procedure [2, 12, 11, 17]. In particle simulations, δf is represented by the numerical markers

$$\delta f = \frac{\langle n \rangle_V V_{\text{tot}}}{N_{\text{mark}}} \sum_{p=1}^{N_{\text{mark}}} \frac{w_p}{J_z} \delta(\mathbf{z} - \mathbf{z}_p) , \quad (7)$$

where N_{mark} is the marker number, $\langle \dots \rangle_V$ indicates the volume average, and V_{tot} is the total volume.

The linearized quasi-neutrality equation in the long-wavelength approximation is as follows,

$$-\nabla \cdot \left(\sum_s \frac{q_s n_{0s}}{B \omega_{cs}} \nabla_{\perp} \delta \Phi \right) = \sum_s q_s \delta n_{s,v} , \quad (8)$$

where the gyrocenter density $\delta n_{s,v}$ is calculated using $\delta f_s(\mathbf{R}, v_{\parallel}, \mu)$ (indicated as $\delta f_{s,v}$), namely, $\delta n_{s,v}(\mathbf{x}) = \int d^6z \delta f_{s,v} \delta(\mathbf{R} + \boldsymbol{\rho} - \mathbf{x})$. Here, \mathbf{x} and \mathbf{R} denote the particle position vector and gyrocenter position vector, respectively, and $\boldsymbol{\rho}$ represents the Larmor radius. In Eq. (8), ω_{cs} is the cyclotron frequency of species s , and in this work, we ignore the perturbed electron polarization density on the left-hand side. When the δf scheme is adopted, $\delta f_{s,v}$ is obtained from $\delta f_{s,u}$ as follows, with the linear approximation of the pullback scheme,

$$\delta f_{s,v} = \delta f_{s,u} + \frac{q_s \langle \delta A_{\parallel}^h \rangle}{m_s} \frac{\partial f_{0s}}{\partial v_{\parallel}} \xrightarrow{\text{Maxwellian}} \delta f_{s,u} - \frac{v_{\parallel}}{T_s} q_s \langle \delta A_{\parallel}^h \rangle f_{0s} . \quad (9)$$

Ampère's law in v_{\parallel} space is $-\nabla_{\perp}^2 \delta A_{\parallel} = \mu_0 \delta j_{\parallel,v}$ where $\delta j_{\parallel,v}(\mathbf{x}) = \sum_s q_s \int d^6z \delta f_{s,v} \delta(\mathbf{R} + \boldsymbol{\rho} - \mathbf{x}) v_{\parallel}$. It is solved in the mixed variable space. Using an iterative scheme [18, 19, 12, 17], the asymptotic solution is expressed as $\delta A_{\parallel}^h = \sum_{I=0}^{\infty} \delta A_{\parallel,I}^h$, where $|\delta A_{\parallel,I+1}^h / \delta A_{\parallel,I}^h| \ll 1$ is assured by the fact that the analytical skin depth term is close to the exact one. Ampère's law is solved iteratively as follows,

$$\left(\nabla_{\perp}^2 - \sum_s \frac{1}{d_s^2} \right) \delta A_{\parallel,0}^h = -\nabla_{\perp}^2 \delta A_{\parallel}^s - \mu_0 \delta j_{\parallel} , \quad (10)$$

$$\left(\nabla_{\perp}^2 - \sum_s \frac{1}{d_s^2} \right) \delta A_{\parallel,I}^h = -\sum_s \frac{1}{d_s^2} \delta A_{\parallel,I-1}^h + \sum_s \frac{1}{d_s^2} \overline{\langle \delta A_{\parallel,I-1}^h \rangle} , \quad (11)$$

$$\overline{\langle \delta A_{\parallel,I-1}^h \rangle} = \frac{2}{n_0 v_{ts}^2} \int dz^6 v_{\parallel}^2 f_{0s} \langle \delta A_{\parallel,I-1}^h \rangle \delta(\mathbf{R} + \boldsymbol{\rho} - \mathbf{x}) \quad \text{for } \delta f , \quad (12)$$

$$\overline{\langle \delta A_{\parallel,I-1}^h \rangle} = \frac{1}{n_0} \int dz^6 f_{s,v} \langle \delta A_{\parallel,I-1}^h \rangle \delta(\mathbf{R} + \boldsymbol{\rho} - \mathbf{x}) \quad \text{for full } f , \quad (13)$$

where $I = 1, 2, 3, \dots$ and details of the δf model and full f model can be found in the previous works [12, 17], $v_{ts} = \sqrt{2T_s/m_s}$, T_s is the temperature, $d_s = c/\omega_{ps}$ is the skin depth, $\omega_{ps} = \sqrt{n_s q_s^2 / (m_s \epsilon_0)}$ is the plasma frequency of species "s".

2.2 Generalized mixed variable-pullback scheme

The original work of the pullback scheme for the δf method can be found in the previous work [11] as follows,

$$\delta A_{\parallel,\text{new}}^s = \delta A_{\parallel,\text{old}}^s + \delta A_{\parallel,\text{old}}^h , \quad (14)$$

$$u_{\parallel,\text{new}} = u_{\parallel,\text{old}} - \frac{q_s}{m_s} \langle \delta A_{\parallel,\text{old}}^h \rangle , \quad (15)$$

$$\delta f_{\text{new}} = \delta f_{\text{old}} + \frac{q_s \langle \delta A_{\parallel,\text{old}}^h \rangle}{m_s} \frac{\partial f_{0s}}{\partial v_{\parallel}} \xrightarrow{\text{Maxwellian}} \delta f_{\text{old}} - \frac{2v_{\parallel}}{v_{ts}^2} \frac{q_s \langle \delta A_{\parallel,\text{old}}^h \rangle}{m_s} f_{0s} , \quad (16)$$

where variables with subscripts "new" and "old" refer to those after and before the pullback transformation, Eq. (16) is the linearized equation for δf pullback, which is from the general equation of the transformation for the distribution function $f_{\text{old}}(u_{\parallel,\text{old}}) = f_{\text{new}}(u_{\parallel,\text{new}})$ ($u_{\parallel,\text{new}} = u_{\parallel,\text{old}} - q_s \langle \delta A_{\parallel,\text{old}}^h \rangle / m_s$). For the full f scheme, only Eqs. (14) and (15) are needed.

Recently, the mixed variable-pullback scheme has been generalized by incorporating the non-ideal Ohm's law that recovers the traditional pure v_{\parallel} scheme and the pure p_{\parallel} scheme [13]. Five schemes have been listed in the generalized pullback scheme, including the original one for which the symplectic part δA_{\parallel}^s is chosen to satisfy ideal Ohm's law involving the electrostatic scalar potential $\delta \Phi$ [11],

$$\partial_t \delta A_{\parallel}^s = -\partial_{\parallel} \delta \Phi , \quad (17)$$

where the parallel derivative is defined as $\partial_{\parallel} = \mathbf{b} \cdot \nabla$, $\mathbf{b} = \mathbf{B}/B$, \mathbf{B} is the equilibrium magnetic field. Another scheme is also implemented in TRIMEG-C1 with

$$\partial_t \delta A_{\parallel}^s = 0 . \quad (18)$$

Note that Eq. (18) is satisfied when solving the field and particle equations during each step before the pullback procedure, while at the end of each step, due to the pullback procedure, the value of δA_{\parallel}^h is shifted to δA_{\parallel}^s and thus, δA_{\parallel}^s becomes nonzero. The scheme with the ideal Ohm's law is suitable for the MHD mode since the physics solution is very close to Eq. (17). For electrostatic modes, such as the ITG mode, Eq. (17) is less efficient. In such a case, Eq. (18) is more suitable, and no field equation for δA_{\parallel}^s needs to be solved. The two schemes are summarized in Tab. 1 while the more general treatment can be found in Tab. I in the previous work [13].

	Equation	Pros
Scheme I	(17)	Good approximation of MHD modes
Scheme II	(18)	No need to solve δA_{\parallel}^s equation; good for electrostatic modes

Table 1. Two schemes implemented in TRIMEG-C1. The other three schemes can be found in [13]. The pure p_{\parallel} scheme solves the system with $\delta A_{\parallel}^h = 0$, which requires a large number of markers and a small time step size and thus is not considered in this work. The pure v_{\parallel} scheme and the mixed variable-pullback scheme with the non-ideal Ohm's law require dedicated effort in implementing the non-ideal Ohm's law and will be studied separately.

3 Piecewise Field-aligned finite element method in triangular meshes

3.1 Traditional 3D finite element method in TRIMEG-C1

The traditional 3D finite element method using C^1 triangular finite elements for the poloidal plane and cubic B-splines in toroidal direction is developed in TRIMEG-C1 as reported in our previous work [5] and is summarized as follows. In the 3D simulation domain Ω , there are N_{vert} vertices in each poloidal plane and N_{ϕ} grids in the toroidal direction. Each poloidal plane is decomposed into N_{tria} triangles. Each triangle is mapped to a reference triangle whose three vertices are $(\xi, \eta) = (0, 0), (1, 0), (0, 1)$, where ξ, η are the reference coordinates. The global coordinates and the reference coordinates can be mapped to each other for a given triangle T_I , namely

$$R = R_I(\xi, \eta), \quad Z = Z_I(\xi, \eta), \quad (19)$$

where (ξ, η) is in the reference triangle, *i.e.* $\xi \in [0, 1], \eta \in [0, 1], \xi + \eta \in [0, 1]$. For linear mappings as adopted in this work, we have $R = (R_{2,I} - R_{1,I})\xi + (R_{3,I} - R_{1,I})\eta + R_{1,I}$, $Z = (Z_{2,I} - Z_{1,I})\xi + (Z_{3,I} - Z_{1,I})\eta + Z_{1,I}$, where $(R_{1,I}, Z_{1,I})$, $(R_{2,I}, Z_{2,I})$ and $(R_{3,I}, Z_{3,I})$ are the coordinates of the three vertices of triangle i . Along the toroidal direction, regular grids and the cubic B-spline are adopted. In each 2D triangle, $N_{\text{bas}} = 18$ basis functions $\Lambda_i(\xi, \eta)$, where $i = 1, \dots, N_{\text{bas}}$, are defined in the reference coordinate (ξ, η) [5].

By applying the continuity condition to the value, the first and second derivatives of the represented function, the degree of freedom in each poloidal plane is reduced from $18N_{\text{tria}}$ to $6N_{\text{vert}}$ before applying the boundary condition. Correspondingly, the three-dimensional variable $Y(R, \phi, Z)$ is written as follows,

$$Y(R, \phi, Z) = \sum_{i=1}^{N_{\text{vert}}} \sum_{j=1}^6 \sum_{k=1}^{N_{\phi}} \widehat{\Lambda}_{ij}(R_I(\xi, \eta), Z_I(\xi, \eta)) \Gamma_k(\phi) \widehat{Y}_{i,j,k}, \quad (20)$$

where $\widehat{\Lambda}_{ij}(R_I(\xi, \eta), Z_I(\xi, \eta))$ are linear combinations of $\Lambda_J(\xi, \eta)$ for $(R, Z) \in T_I$ (Eq. (73) of [5]). Here the index J between 1 and N_{bas} depends on the vertex i and the triangle I through the mapping. Due to this construction, the support of $\widehat{\Lambda}_{i,j}$ corresponds to all the triangles with vertex i and $\widehat{\Lambda}_{i,j}$ is in C^1 . On the other hand $\Gamma_k(\phi)$ is the cubic spline basis function, and N_{ϕ} is the grid point number in the toroidal direction. Since there is a one-to-one mapping between the reference coordinates (ξ, η) and the global coordinates (R, Z) in each triangle as indicated by Eq. (19), Eq. (20) can be also written as

$$Y(R, \phi, Z) = \sum_{i=1}^{N_{\text{vert}}} \sum_{j=1}^6 \sum_{k=1}^{N_{\phi}} \widehat{\Lambda}_{ij}(R, Z) \Gamma_k(\phi) \widehat{Y}_{i,j,k}. \quad (21)$$

The weak form of the equation to be solved, needed for a finite element formulation, can be obtained by multiplying it by the test function $\widehat{\Lambda}_{i',j'}(R, Z) \Gamma_{k'}(\phi)$ and calculating the volume integral in the simulation domain. The coefficients $\widehat{Y}_{i,j,k}$ can be obtained from the weak form and are used for calculating the field at the particle location for pushing particles. More details can be found in the previous work [5].

3.2 Piecewise field-aligned finite element method in (R, ϕ, Z) coordinates

The piecewise field-aligned finite element method (PFAFEM) has been proposed to study the multi-harmonic nonlinear physics in tokamak plasmas with increased computational efficiency. Previously, it has been implemented in the electrostatic particle model for the core plasma in the tokamak coordinate (r, ϕ, θ) , where r , ϕ , and θ are the radial-like, toroidal-like, and poloidal-like coordinates [6]. In this work, the PFAFEM has been extended and implemented in cylindrical coordinates for electromagnetic whole-volume simulations. The two key features of the PFAFEM still hold:

1. The computational grids are aligned in a traditional pattern without any shift.
2. The finite element basis functions are defined on piecewise field-aligned coordinates, with each basis function being continuous along the magnetic field line.

The previous treatment of PFAFEM in (r, ϕ, θ) is summarized as follows [6]. We first defined the k 'th subdomain as

$$\phi - \phi_k \in [-N_{\text{bsp}}\Delta\phi/2, N_{\text{bsp}}\Delta\phi/2] \quad (22)$$

where $\phi_k = (k - 1)\Delta\phi$ is the coordinate of the toroidal grid point, $\Delta\phi$ is the toroidal grid spacing, and N_{bsp} is the order of the B-Spline (for cubic B-spline, $N_{\text{bsp}} = 4$). In (r, ϕ, θ) coordinates, the safety factor is $q(r, \theta) \equiv \mathbf{B} \cdot \nabla\phi / (\mathbf{B} \cdot \nabla\theta)$. The piecewise field-aligned local coordinate η_k is defined in each toroidal subdomain centered at ϕ_k grid as $\eta_k(r, \theta, \phi) = \theta - \int_{\phi_k}^{\phi} d\phi' / q(r, \theta'(r, \phi'), \phi')$, where the integral is along the magnetic field line and the safety factor $q = q(r, \theta', \phi')$, θ' is determined by following the magnetic field while varying ϕ' , namely, $d\theta'/d\phi' = 1/q(r, \theta', \phi')$, ϕ_k and ϕ denote the starting and end points of the integral, respectively. For the straight field line coordinates $r, \bar{\theta}, \bar{\phi}$, we have $\eta_k(r, \bar{\theta}, \bar{\phi}) = \bar{\theta} - (\bar{\phi} - \bar{\phi}_k)/\bar{q}$, where the safety factor $\bar{q} = \bar{q}(r)$. More details can be found in the previous work [6].

In this work, for the whole volume simulation, we construct two field-aligned coordinates R_{FA} and Z_{FA} , by tracing the equilibrium magnetic field lines. The subdomain is defined in Eq. (22). The piecewise field-aligned local coordinate $R_{\text{FA},k}$ and $Z_{\text{FA},k}$ are defined in each toroidal subdomain centered at ϕ_k grid as follows,

$$R_{\text{FA},k}(R, Z, \phi) = R - \int_{\phi_k}^{\phi} d\phi' \frac{\mathbf{b} \cdot \nabla R'}{\mathbf{b} \cdot \nabla\phi'} , \quad (23)$$

$$Z_{\text{FA},k}(R, Z, \phi) = Z - \int_{\phi_k}^{\phi} d\phi' \frac{\mathbf{b} \cdot \nabla Z'}{\mathbf{b} \cdot \nabla\phi'} , \quad (24)$$

where the integral is along the magnetic field line. Numerically, $R_{\text{FA},k}$ and $Z_{\text{FA},k}$ are calculated on the 3D grids (R_I, Z_J, ϕ_K) and stored as 3D matrices $R_{\text{FA},k,IJK}$ and $Z_{\text{FA},k,IJK}$. The values of $R_{\text{FA},k}$ and $Z_{\text{FA},k}$ on each grid point (R_I, Z_J, ϕ_K) is calculated by solving the characteristic line from ϕ_K to the middle toroidal position ϕ_k of the subdomain, namely, the ϕ coordinate of toroidal grids, using the Runge-Kutta 4th order scheme,

$$\frac{dR_{\text{FA},k}}{d\phi} = \frac{\mathbf{b} \cdot \nabla R}{\mathbf{b} \cdot \nabla\phi} , \quad (25)$$

$$\frac{dZ_{\text{FA},k}}{d\phi} = \frac{\mathbf{b} \cdot \nabla Z}{\mathbf{b} \cdot \nabla\phi} , \quad (26)$$

which is called ‘backward field line tracing’ since the direction of the integral is from ϕ back to the reference toroidal location ϕ_k . Then with $R_{\text{FA},k,IJK}$ and $Z_{\text{FA},k,IJK}$, the values of $R_{\text{FA},k}$ and $Z_{\text{FA},k}$ at a given position (R, Z, ϕ) can be obtained by B-spline interpolation.

The piecewise field-aligned finite element basis function is defined in $(R_{\text{FA},k}, \phi, Z_{\text{FA},k})$. A perturbed field variable Y is represented as the summation of these field-aligned finite element basis functions as follows,

$$Y(R, \phi, Z) = \sum_{i=1}^{N_{\text{vert}}} \sum_{j=1}^6 \sum_{k=1}^{N_{\phi}} \widehat{\Lambda}_{i,j}(R_{\text{FA},k}, Z_{\text{FA},k}) \Gamma_k(\phi) \widehat{Y}_{i,j,k} . \quad (27)$$

Compared with the traditional 3D finite element method in Eq. (21), the difference is that using PFAFEM, $\widehat{\Lambda}$ is defined in $(R_{\text{FA},k}, Z_{\text{FA},k})$ instead of (R, Z) . The interpolation of the perturbed field

at the particle location (“gathering”) can be performed in $(R_{\text{FA},k}, \phi, Z_{\text{FA},k})$ using Eq. (27). The derivative is calculated using the chain rule,

$$\frac{\partial}{\partial R} Y(R, \phi, Z) = \sum_{i=1}^{N_{\text{vert}}} \sum_{j=1}^6 \sum_{k=1}^{N_{\phi}} \left(\frac{\partial R_{\text{FA}}}{\partial R} \frac{\partial}{\partial R_{\text{FA},k}} \hat{\Lambda}_{i,j} + \frac{\partial Z_{\text{FA}}}{\partial R} \frac{\partial}{\partial Z_{\text{FA},k}} \hat{\Lambda}_{i,j} \right) \Gamma_k(\phi) \hat{Y}_{i,j,k} , \quad (28)$$

$$\frac{\partial}{\partial Z} Y(R, \phi, Z) = \sum_{i=1}^{N_{\text{vert}}} \sum_{j=1}^6 \sum_{k=1}^{N_{\phi}} \left(\frac{\partial R_{\text{FA}}}{\partial Z} \frac{\partial}{\partial R_{\text{FA},k}} \hat{\Lambda}_{i,j} + \frac{\partial Z_{\text{FA}}}{\partial Z} \frac{\partial}{\partial Z_{\text{FA},k}} \hat{\Lambda}_{i,j} \right) \Gamma_k(\phi) \hat{Y}_{i,j,k} , \quad (29)$$

$$\begin{aligned} \frac{\partial}{\partial \phi} Y(R, \phi, Z) = & \sum_{i=1}^{N_{\text{vert}}} \sum_{j=1}^6 \sum_{k=1}^{N_{\phi}} \left[\left(\frac{\partial R_{\text{FA}}}{\partial \phi} \frac{\partial}{\partial R_{\text{FA},k}} \hat{\Lambda}_{i,j} + \frac{\partial Z_{\text{FA}}}{\partial \phi} \frac{\partial}{\partial Z_{\text{FA},k}} \hat{\Lambda}_{i,j} \right) \Gamma_k(\phi) \right. \\ & \left. + \hat{\Lambda}_{i,j} \frac{\partial}{\partial \phi} \Gamma_k(\phi) \right] \hat{Y}_{i,j,k} , \end{aligned} \quad (30)$$

where we have omitted the arguments in $\hat{\Lambda} = \hat{\Lambda}(R_{\text{FA},k}, Z_{\text{FA},k})$. In the implementation, Eqs. (28)–(30) are adopted to calculate the spatial derivatives of $\delta\Phi$ and δA_{\parallel} in the R, ϕ, Z directions to push particles in (R, ϕ, Z) coordinates.

The calculation of the perturbed density and parallel current (“scattering”) is obtained by the projection operator from particles to the field-aligned finite element basis functions, as to be introduced in Section 3.3.

The partition of unity is obtained readily for the traditional 3D scheme. In the poloidal plane, noting that Λ_1 , Λ_7 , and Λ_{13} are associated with the values of the function while the other basis functions are associated with the derivatives, the partition of unity is $\Lambda_1 + \Lambda_7 + \Lambda_{13} = 1$. To prove it, first, write each term in a symmetric way, $\Lambda_1 = 10\lambda^3 - 15\lambda^4 + 6\lambda^5 + 30\lambda^2\xi\eta(\xi + \eta)$, $\Lambda_7 = 10\xi^3 - 15\xi^4 + 6\xi^5 + 15\xi^2\eta^2\lambda$, $\Lambda_{13} = 10\eta^3 - 15\eta^4 + 6\eta^5 + 15\xi^2\eta^2\lambda$. Then the summation yields $\Lambda_1 + \Lambda_7 + \Lambda_{13} = 10(\lambda^3 + \xi^3 + \eta^3) - 15(\lambda^4 + \xi^4 + \eta^4) + 6(\lambda^5 + \xi^5 + \eta^5) + 30\lambda^2\xi\eta(\xi + \eta) + 30\xi^2\eta^2\lambda$ [5]. After expanding and collecting terms, using $\lambda = 1 - \xi - \eta$, the expression reduces to the constant 1. Then also noting Eqs. (73) and (74) in our previous work [5], we have

$$\hat{\Lambda}_{i_1,1} + \hat{\Lambda}_{i_2,1} + \hat{\Lambda}_{i_3,1} = 1 , \quad (31)$$

where i_1, i_2, i_3 are the three vertices of a triangle, and $\hat{\Lambda}_{i_1,1} = \Lambda_1$, $\hat{\Lambda}_{i_1,2} = \Lambda_7$, $\hat{\Lambda}_{i_1,3} = \Lambda_{13}$.

For traditional 3D FEM, the partition of unity is proved as follows,

$$\sum_{k=1}^{N_{\phi}} \left[\hat{\Lambda}_{i_1,1}(R_p, Z_p) + \hat{\Lambda}_{i_2,1}(R_p, Z_p) + \hat{\Lambda}_{i_3,1}(R_p, Z_p) \right] \Gamma_k(\phi_p) = \sum_{k=1}^{N_{\phi}} \Gamma_k(\phi_p) = 1 , \quad (32)$$

where (R_p, ϕ_p, Z_p) denote the particle location.

For the piecewise field-aligned FEM,

$$\sum_{k=1}^{N_{\phi}} \Gamma_k(\phi_p) \left[\hat{\Lambda}_{i_1,1}(R_{p,k}, Z_{p,k}) + \hat{\Lambda}_{i_2,1}(R_{p,k}, Z_{p,k}) + \hat{\Lambda}_{i_3,1}(R_{p,k}, Z_{p,k}) \right] = \sum_{k=1}^{N_{\phi}} \Gamma_k(\phi_p) = 1 , \quad (33)$$

since $\hat{\Lambda}_{i_1,1}(R_{p,k}, Z_{p,k}) + \hat{\Lambda}_{i_2,1}(R_{p,k}, Z_{p,k}) + \hat{\Lambda}_{i_3,1}(R_{p,k}, Z_{p,k}) = 1$ applies for a given value of k and the particle location. The partition of unity has also been discussed and proved previously in the mesh-free scheme [20]. It can be readily demonstrated that Eqs. (32) and (33) ensure charge (particle-number) conservation in the projection operator in Eqs. (39) and (46).

The constructed $(R_{\text{FA},k}, Z_{\text{FA},k})$ grids are demonstrated in Fig. 1. It corresponds to the TCV-X21 [21, 22, 23] case used for the numerical studies in Section 4. The coordinates $(R_{\text{FA},k}, Z_{\text{FA},k})$ are evaluated on the sub-grids in each toroidal subdomain. Then $(R_{\text{FA},k}, Z_{\text{FA},k})$ are numerically represented as functions of (R, Z, ϕ) . The grid in $(R_{\text{FA},k}, Z_{\text{FA},k})$ is distorted more strongly as the toroidal location is farther away from the mid location of the toroidal subdomain, as demonstrated in Fig. 1. This also demonstrates a key advantage of PFAFEM in mitigating grid distortion, which becomes severe when global field-aligned coordinates are used. By constructing $(R_{\text{FA},k}, Z_{\text{FA},k})$ locally within each toroidal subdomain $\phi - \phi_k \in [-N_{\text{bsp}}\Delta\phi/2, N_{\text{bsp}}\Delta\phi/2]$, the resulting distortion is significantly reduced compared to that over the full toroidal domain $[0, 2\pi]$, where magnetic shear has a more pronounced effect on the grid distortion. Furthermore, via a higher number of toroidal finite elements, the grid distortion can be reduced to the required level.

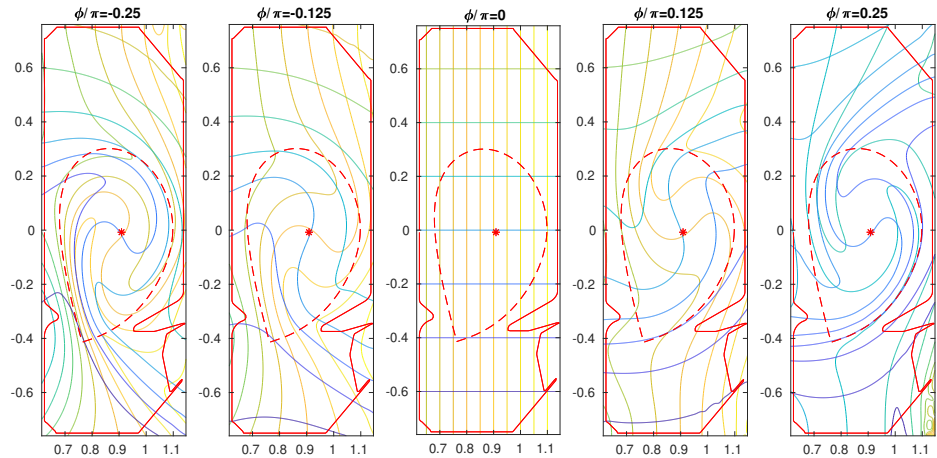


Figure 1. The grid of the piecewise field-aligned coordinates ($R_{\text{FA}}, Z_{\text{FA}}$) (Section 3.2).

3.3 The 3D traditional and the PFAFEM field solvers

Four field equations are solved: the quasi-neutrality equation, Ampère's law, the iterative Ampère equation, and Ohm's law. We first discuss the general form of the field equation and later demonstrate the four field equations separately. The general form of the field equation is

$$M_L \cdot \mathbf{y} = \mathbf{b} + M_R \cdot \mathbf{c} , \quad (34)$$

where M_L and M_R are partial differential operators, \mathbf{b} and \mathbf{c} are known vectors, \mathbf{y} is the vector to be solved, and the physics variable b corresponding to the vector \mathbf{b} is calculated from the particle distribution function,

$$b = \int d^3v \delta f Q(\mathbf{v}) , \quad (35)$$

where $Q(\mathbf{v})$ is a function of the velocity (for the quasi-neutrality equation, $Q(\mathbf{v}) = 1$; for Ampère's law, $Q(\mathbf{v}) = v_{\parallel}$). The corresponding general matrix form of the field equations is

$$\bar{M}_{L,ii',jj',kk'} \cdot Y_{i'j'k'} = B^{i,j,k} + \bar{M}_{R,ii',jj',kk'} \cdot C_{i'j'k'} , \quad (36)$$

$$\bar{M}_{L/R,ii',jj',kk'} = \int dR dZ d\phi J \Upsilon_{ijk} M_{L/R} \Upsilon_{i'j'k'} , \quad (37)$$

where $Y_{i'j'k'}$ is the field variable to be solved by the linear solver, $B^{i,j,k}$ is from the markers using the projection operator, $C_{i'j'k'}$ is the known field variable, $\bar{M}_{L,ii',jj',kk'}$ and $\bar{M}_{R,ii',jj',kk'}$ are the matrices on the left- and right-hand sides, respectively. The 3D basis functions Υ_{ijk} and $\Upsilon_{i'j'k'}$ denote those in (R, ϕ, Z) coordinate for the traditional solver or those in $(R_{\text{FA}}, \phi, Z_{\text{FA}})$ coordinate for the PFAFEM solver. We will list them separately below.

For the traditional 3D FEM solver,

$$\Upsilon_{ijk} = \Upsilon_{ijk}(R, Z, \phi) = \hat{\Lambda}_{ij}(R, Z) \Gamma_k(\phi) , \quad (38)$$

$$B^{i,j,k} = \sum_s C_{\text{p2g},s} \sum_{p=1}^{N_{\text{mark}}} w_p Q(\mathbf{v}_p) \Upsilon_{ijk}(R_p, Z_p, \phi_p) , \quad (39)$$

where the conversion factor in the projection operator $C_{\text{p2g},s} = -\bar{q}_s \langle n \rangle_V V_{\text{tot}} / N_{\text{mark}}$.

The matrix is calculated using a modified Gauss quadrature. The general form of the matrix in $\bar{M}_{L/R,ii',jj',kk'}$ contains the volume integral after the integral by parts when $M_{L/R}$ is a second (or higher) order differential operator,

$$m_{ii',jj',kk'} = \int dr d\theta d\phi J L_1 \Upsilon_{ijk} L_2 \Upsilon_{i'j'k'} , \quad (40)$$

where L_1 and L_2 are differential operators associated to $M_{L/R}$. For example, for $M_{L/R} = \partial^2 / \partial R^2$, we have $L_1 = -\partial / \partial R$ and $L_2 = \partial / \partial R$. Using the modified Gauss quadrature in prisms

$$m_{ii',jj',kk'} = \sum_{I=1}^{I_{\text{max}}} \sum_{J=1}^{J_{\text{max}}} J L_1 \Upsilon_{ijk}(R_I, \phi_J, Z_I) L_2 \Upsilon_{i'j'k'}(R_I, \phi_J, Z_I) , \quad (41)$$

where I and J denote the indices of the quadrature points in the reference coordinate (ξ, η) and in the toroidal direction, respectively.

The toroidal filter can be applied to single- n simulations in the traditional 3D solver, following the previous approach for deriving the 2D filter [17], and then reduced to the 1D toroidal filter. The toroidal harmonic is kept as follows,

$$b(R, \phi, Z) = b_n(R, Z)e^{in\phi} + \text{c.c.} \quad (42)$$

where c.c. denotes the complex conjugate $b_{-n}(R, Z)e^{-in\phi}$ for nonzero n while for $n = 0$, c.c. is zero. To apply the toroidal Fourier filter to the coefficient $B^{i,j,k}$, we first calculate the Fourier component as follows,

$$b_{ijn} = \frac{C_{\text{p2g},s}}{\phi_{\text{wid}}} \sum_{p=1}^{N_{\text{mark}}} w_p Q(\mathbf{v}) e^{-in\phi_p} \widehat{\Lambda}_{ij}(R_p, Z_p) \quad (43)$$

Then Eq. (38) is replaced with

$$B_{\text{filter}}^{i,j,k} = \sigma_n \text{Re}(T_{n,k} e^{in\phi_k}) \Delta\phi b_{ijn} \quad (44)$$

where $\sigma_n = 2$ for $n \neq 0$ and $\sigma_n = 1$ for $n = 0$, $T_{n,k} = [6 + 2\cos(2n_{\text{eff}}) - 8\cos(n_{\text{eff}})]/n_{\text{eff}}^4 = [2\sin(n_{\text{eff}}/2)/n_{\text{eff}}]^4$ for $n \neq 0$ and $T_{n,k} = 1$ for $n = 0$, $n_{\text{eff}} = n\Delta\phi$.

For the 3D field-aligned FEM solver,

$$\Upsilon_{ijk} = \Upsilon_{ijk}(R_{\text{FA},k}, Z_{\text{FA},k}, \phi) = \widehat{\Lambda}_{ij}(R_{\text{FA},k}, Z_{\text{FA},p,k}) \Gamma_k(\phi) \quad (45)$$

$$B^{i,j,k} = \sum_s C_{\text{p2g},s} \sum_{p=1}^{N_{\text{mark}}} w_p Q(\mathbf{v}_p) \Upsilon_{ijk}(R_{\text{FA},p,k}, Z_{\text{FA},p,k}, \phi_p) \quad (46)$$

The matrix is calculated using the modified Gauss quadrature and the mixed particle-wise-basis-wise scheme [6] but expressed in $(R_{\text{FA}}, \phi, Z_{\text{FA}})$ coordinates. The integral points $(R_{\text{FA},I,k}, \phi_J, Z_{\text{FA},I,k})$ are determined in the basis function Υ_{ijk} (grid-wise), and the corresponding $(R_{I,k}, \phi_J, Z_{I,k})$ are calculated to determine the integral points in $\Upsilon_{i'j'k'}$ (particle-wise). The matrix element is calculated as follows,

$$m_{ii',jj',kk'} = \sum_{I=1}^{I_{\text{max}}} \sum_{J=1}^{J_{\text{max}}} J L_1 \Upsilon_{ijk}(R_{\text{FA},I,k}, \phi_J, Z_{\text{FA},I,k}) L_2 \Upsilon_{i'j'k'}(R'_{\text{FA},I,k'}, \phi_J, Z'_{\text{FA},I,k'}) \quad (47)$$

where $R'_{\text{FA},I,k'}$ and $Z'_{\text{FA},I,k'}$ are determined by

$$R(R'_{\text{FA},I,k'}, \phi_J - \phi_{k'}, Z'_{\text{FA},I,k'}) = R(R_{\text{FA},I,k}, \phi_J - \phi_k, Z_{\text{FA},I,k}) \quad (48)$$

$$Z(R'_{\text{FA},I,k'}, \phi_J - \phi_{k'}, Z'_{\text{FA},I,k'}) = Z(R_{\text{FA},I,k}, \phi_J - \phi_k, Z_{\text{FA},I,k}) \quad (49)$$

since each integral point is identical regardless of the coordinate system.

3.4 Weak form of the field equations

To express the weak form of the field equations, we first give the normalized forms. The normalized quasi-neutrality equation is,

$$\bar{\nabla}_{\perp} \cdot (G_{\text{P}} \bar{\nabla}_{\perp} \delta \bar{\Phi}) = -C_{\text{P}} \delta \bar{N} \quad , \quad G_{\text{P}} = \sum_s \frac{n_{0s}}{n_{\text{ref}}} \bar{m}_s \left(\frac{B_{\text{N}}}{B} \right)^2 \quad , \quad (50)$$

where $C_{\text{P}} = 1/\bar{\rho}_{\text{ref}}^2$, $\delta \bar{N}_s = \delta n / n_{\text{ref}}$, $\delta \bar{N} = \sum_s \bar{q}_s \delta \bar{N}_s$.

The normalized Ampère's law and the iterative scheme corresponding to Eqs. (10)–(13),

$$\left(\bar{\nabla}_{\perp}^2 - \sum_s \frac{\bar{q}_s^2}{\bar{m}_s} C_{\text{A}} \right) \delta \bar{A}_{\parallel,0}^{\text{h}} = -\bar{\nabla}_{\perp}^2 \delta \bar{A}_{\parallel,0}^{\text{s}} - C_{\text{A}} \delta \bar{J}_{\parallel} \quad , \quad (51)$$

$$\left(\bar{\nabla}_{\perp}^2 - \sum_s \frac{\bar{q}_s^2}{\bar{m}_s} C_{\text{A}} \right) \delta \bar{A}_{\parallel,I}^{\text{h}} = -\sum_s \frac{\bar{q}_s^2}{\bar{m}_s} C_{\text{A}} \delta \bar{A}_{\parallel,I-1}^{\text{h}} + \bar{G} \delta \bar{A}_{\parallel,I-1}^{\text{h}} \quad (52)$$

$$\bar{G} \delta \bar{A}_{\parallel,I-1}^{\text{h}} = C_{\text{A}} \frac{N_{0s} \bar{q}_s^2}{\bar{T}_s} \sum_{p=1}^N 2 \bar{v}_{\parallel,p}^2 \int dz^6 w_p \delta(\tilde{\mathbf{R}}_p) \langle \delta \bar{A}_{\parallel,I-1}^{\text{h}} \rangle \text{ for } \delta f \quad , \quad (53)$$

$$\bar{G} \delta \bar{A}_{\parallel,I-1}^{\text{h}} = C_{\text{A}} \frac{N_{0s} \bar{q}_s^2}{\bar{m}_s} \sum_{p=1}^N \int dz^6 p_{p,\text{tot}} \delta(\tilde{\mathbf{R}}_p) \langle \delta \bar{A}_{\parallel,I-1}^{\text{h}} \rangle \text{ for full } f \quad , \quad (54)$$

where $\tilde{\mathbf{R}}_p = \mathbf{R}_p + \rho_p - \mathbf{x}$, $\rho_p = m_s \mathbf{v}_{\perp,p} / (q_s B)$, \mathbf{x} denotes the particle location, $C_A = \beta_{\text{ref}} / \rho_{\text{ref}}^2$, n_{ref} is the reference density and is chosen as the electron density on magnetic axis, and $\delta \bar{J}_{\parallel} = \delta j_{\parallel} / (e v_N n_{\text{ref}})$.

The Ohm's law is

$$\partial_t \delta \bar{A}_{\parallel}^s = \begin{cases} -\partial_{\parallel} \delta \bar{\Phi} & , \text{ scheme I,} \\ 0 & , \text{ scheme II.} \end{cases} \quad (55)$$

The weak form is expressed as follows

$$(50) \Rightarrow \bar{M}_{P,L,ii',jj',kk'} \cdot \delta \Phi_{i'j'k'} = C_P \int dR dZ d\phi J \delta N^{i,j,k} \Upsilon_{ijk} , \quad (56)$$

$$(51) \Rightarrow \bar{M}_{A,L,ii',jj',kk'} \cdot \delta A_{i'j'k',I=0}^h = \bar{M}_{A,R,ii',jj',kk'} \cdot \delta A_{i'j'k'}^s + C_A \delta J_{\parallel}^{i,j,k} , \quad (57)$$

$$(52) \Rightarrow \bar{M}_{it,L,ii',jj',kk'} \cdot \delta A_{i'j'k',I+1}^h = \bar{M}_{it,R,ii',jj',kk'} \cdot \delta A_{i'j'k',I}^h + \sum_s \frac{1}{d_s^2} \overline{\langle \delta A_{i,j,k,I}^h \rangle} , \quad (58)$$

$$(55) \Rightarrow \bar{M}_{\text{Ohm},L,ii',jj',kk'} \cdot \partial_t \delta A_{i'j'k'}^s = \bar{M}_{\text{Ohm},R,ii',jj',kk'} \cdot \delta \Phi_{i'j'k'} \quad \text{for scheme I .} \quad (59)$$

For scheme II, we do not need to solve any Ohm's law. Equations (56)–(59) are solved numerically which provides the perturbed fields for solving the gyro center's equations of motion. Homogeneous Dirichlet boundary conditions are applied by setting the boundary values to zero. The matrices and the terms on the right-hand side are as follows,

$$\begin{aligned} \bar{M}_{P,L,ii',jj',kk'} &= - \sum n_{0s} \bar{m}_s \frac{B_{\text{ref}}^2}{B^2} \int dR dZ d\phi J \nabla_{\perp} \Upsilon_{ijk} \cdot \nabla_{\perp} \Upsilon_{i'j'k'} , \\ \delta N^{i,j} &= - \sum \bar{q}_s \int dR dZ d\phi J \delta \bar{N}_s(R, \phi, Z) \Upsilon_{ijk} , \\ \bar{M}_{A,L,ii',jj',kk'} &= \int dR dZ d\phi J \left(-\nabla_{\perp} \Upsilon_{ijk} \cdot \nabla_{\perp} \Upsilon_{i'j'k'} - \sum_s \frac{\bar{q}_s^2}{\bar{m}_s} C_A \Upsilon_{ijk} \Upsilon_{i'j'k'} \right) , \\ \bar{M}_{A,R,ii',jj',kk'} &= \int dR dZ d\phi J \nabla_{\perp} \Upsilon_{ijk} \cdot \nabla_{\perp} \Upsilon_{i'j'k'} , \\ \delta J_{\parallel}^{i,j} &= - \int dR dZ d\phi J \delta \bar{J}_{\parallel}(R, \phi, Z) \Upsilon_{ijk} , \\ \bar{M}_{it,L,ii',jj',kk'} &= \bar{M}_{A,L,ii',jj',kk'} , \\ \overline{\langle \delta A_{i,j,I}^h \rangle} &= \int dR dZ d\phi J \overline{\langle \delta A_I^h \rangle} \Upsilon_{ijk} , \\ \bar{M}_{it,R,ii',jj',kk'} &= - C_A \sum_s \frac{\bar{q}_s^2}{\bar{m}_s} \int dR dZ d\phi J \Upsilon_{ijk} \Upsilon_{i'j'k'} , \\ \bar{M}_{\text{Ohm},L,ii',jj',kk'} &= \int dR dZ d\phi J \Upsilon_{ijk} \Upsilon_{i'j'k'} , \\ \bar{M}_{\text{Ohm},R,ii',jj',kk'} &= - \int dR dZ d\phi J \Upsilon_{ijk} \partial_{\parallel} \Upsilon_{i'j'k'} , \end{aligned} \quad (60)$$

where Υ_{ijk} is chosen as the traditional 3D basis function or the piecewise field-aligned basis function as discussed in Section 3.3.

4 Simulation results

4.1 Parameters and setup of the TCV-X21 case

The TCV-X21 case has been studied experimentally and numerically for Tokamak à configuration variable (TCV) [21, 22, 23]. This case is used by various codes such as GRILLIX and GENE-X for the studies of the transport and the profile generation with the consideration of the separatrix. The simulation starts from the EQDSK file that gives the poloidal flux function ψ_p , and other profiles and parameters such as the safety factor $q(\psi_p)$. The upper left frame of Fig. 2 shows the poloidal flux function ψ_p where the solid and dashed red lines indicate the vessel surface and the plasma separatrix, respectively. The profile of the safety factor is shown in the lower left frame. The simulation domain is chosen as shown in the upper right frame. The triangular mesh is plotted with reduced resolution (1476 vertices) compared to that used in the simulations (5037 vertices) for better visibility. The vertices of the triangular mesh are aligned with the flux surfaces, with additional refinement applied

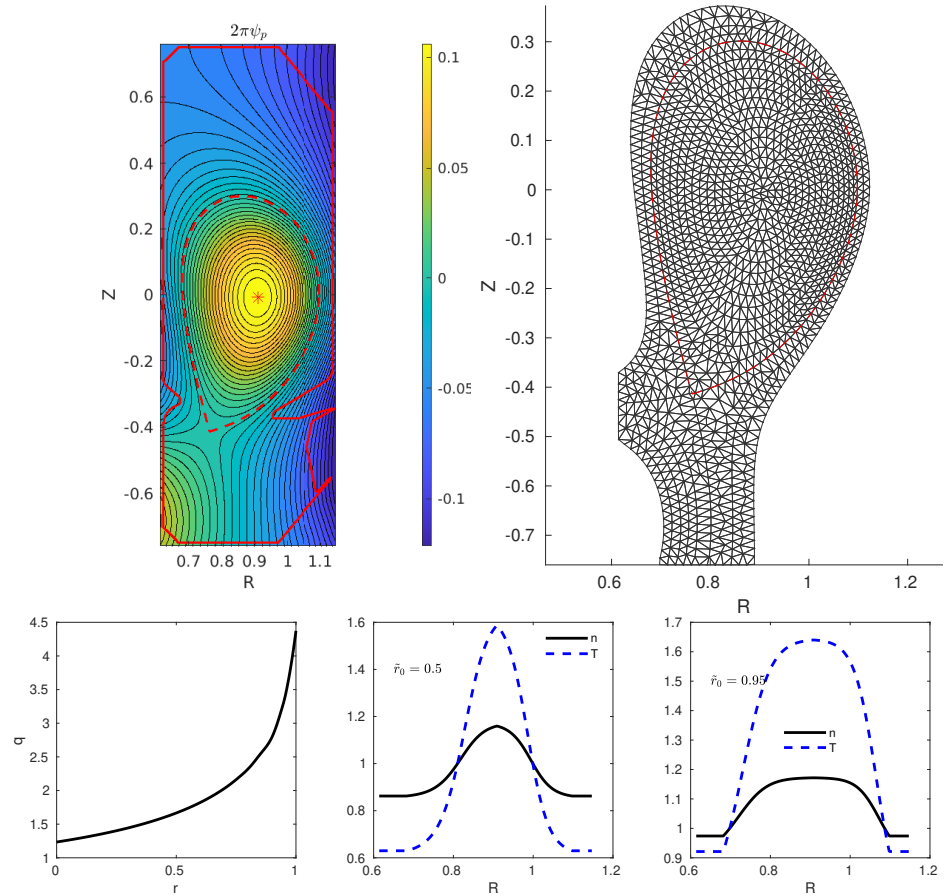


Figure 2. The poloidal flux function $2\pi\psi_p$ (upper left); the simulation domain with triangular meshes (upper right); the safety factor profile (lower left); the density and temperature (n, T) profiles along R at $Z = Z_{\text{axis}}$ for simulations of the core instability (lower middle) and the edge instability (lower right). The density and temperature are normalized to n_{ref} and T_{ref} , respectively (Section 4.1).

in the open field line region, especially in the vicinity of the X-point, to accurately capture the complex geometry.

The simulation is performed in this section to demonstrate the basic features of the linear ITG instability in the presence of the open field lines. For single- n simulations, the particle-in-Fourier scheme is adopted in calculating the density and the current perturbation, but converted to the finite element space before the field equations are solved [7]. The reference plasma beta $\beta_{\text{ref}} = \mu_0 n_{\text{ref}} m_N v_N^2 / B_{\text{ref}}^2$ and the reference Larmor radius $\rho_{\text{ref}} = m_N v_N / (e B_{\text{ref}})$, where m_N is the proton mass, $v_N = \sqrt{2T_{\text{ref}}/m_N}$, and the subscripts “ N ” and “ ref ” denote the normalization unit and some reference parameter-value in the TRIMEG-C1 code. The reference magnetic field is $B_{\text{ref}} = 1$ T while the on-axis magnetic field is $B_{\text{axis}} = 0.90727$ T. The reference density and temperature are $n_{\text{ref}} = 3.5 \times 10^{19}/m^3$ and $T_{\text{ref}} = 600$ eV, respectively, at the reference radial location $\tilde{r}_0 = 0$. Correspondingly, the reference Larmor radius is $\rho_{\text{ref}} = 0.3539$ cm and reference beta is $\beta_{\text{ref}} = 0.84561\%$. More details of the normalization in TRIMEG-C1 are in the previous work [17, 5]. The ion-to-electron mass ratio used is 100. The equilibrium density and temperature profiles $H(\tilde{r})$, with $H = n$ or T , are given by

$$\frac{H(\tilde{r})}{H(\tilde{r}_0)} = \exp \left[-\kappa_H w_H \frac{\tilde{a}}{R_0} \tanh \left(\frac{\tilde{r} - \tilde{r}_0}{w_H} \right) \right], \quad (61)$$

where $\tilde{r} = \sqrt{(\psi - \psi_{\text{axis}})/(\psi_{\text{edge}} - \psi_{\text{axis}})}$, $\kappa_T = 6.96$, $\kappa_n = 2.23$, the center of the simulation domain $R_0 = 0.88$ m, $\tilde{a} = (R_{\text{sep,max}} - R_{\text{sep,min}})/2 = 0.20926$ m, R_{sep} is the R coordinate of the separatrix, and $w_{n,T} = 0.3$. To study the instabilities destabilized in the core plasma and near the separatrix, we selected $\tilde{r}_0 = 0.5$ and 0.95, respectively. The density and temperature are assumed to be constant outside of the separatrix in this work for the sake of simplicity. The equilibrium ion and electron profiles are assumed to be identical. The density and the temperature profiles are shown in the lower frame of Fig. 7. The finite Larmor radius effect is omitted in this work. To study features of the instabilities with different normalized machine size a/ρ_{ref} , another case with $\rho_{\text{ref}} = 0.01$ m is chosen,

which corresponds to $n_{\text{ref}} = 0.43847 \times 10^{19}/\text{m}^3$ and $T_{\text{ref}} = 4789.4 \text{ eV}$. Four cases studied in the following subsections are summarized in Tab. 2. In the following, Sections 4.2–4.4 concentrate on the analysis of linear properties, while Section 4.5 addresses the non-linear dynamics.

	ρ_{ref} (cm)	\tilde{r}_0
1a	0.3539	0.5
1b	0.3539	0.95
2a	1.0	0.5
2b	1.0	0.95

Table 2. Four cases with different values of ρ_{ref} and \tilde{r}_0 are used for the numerical studies of the TCV-X21 scenario.

4.2 Electromagnetic instabilities in the core and near separatrix

To demonstrate the performance of TRIMEG-C1 for electromagnetic simulations, the instabilities in the core and near the separatrix are simulated using the parameters 1a and 1b in Tab. 2. The 2D mode structures of $\delta\phi$ and δA_{\parallel} are displayed in Fig. 3 for the $n = 10$ mode with $\rho_{\text{ref}} = 0.3539 \text{ cm}$. The time step size is $\Delta t/t_N = 0.001$ where t_N is the time unit of the TRIMEG-C1 code [5, 7]. The results for gradient-driven instabilities in the core are shown in the upper panel of Fig. 3 (case 1a), while those for the edge region near the separatrix are presented in the lower panel (case 1b). In case 1a, where the density and temperature gradients are located at $\tilde{r}_0 = 0.5$, the electrostatic potential fluctuation $\delta\phi$ exhibits a clear ballooning structure, while the magnitude of the parallel magnetic potential δA is lower at the low field side, due to the different property between δA and $\delta\phi$ along the magnetic field line. The perturbation $\delta\phi$ typically peaks near $\theta = 0$ and exhibits even parity with respect to $\theta = 0$ along the magnetic field line, leading to localization at the outboard midplane. However, for ITG mode, δA_{\parallel} tends to have an odd parity with respect to $\theta = 0$ along the magnetic field line, resulting in a reduced amplitude at the low-field-side midplane, which is common in Alfvénic or electrostatic micro-scale instabilities [24, 25, 26].

In case 1b, where the gradients are shifted outward to $\tilde{r}_0 = 0.95$ near the separatrix, both $\delta\phi$ and δA_{\parallel} are localized closer to the plasma separatrix and become more radially extended. Compared to the core case, the modes near the separatrix display poloidal variation and finer-scale structure, reflecting the enhanced magnetic shear effects in the edge region. The relative magnitude of δA_{\parallel} compared with $\delta\phi$ remains comparable between cases 1a and 1b, indicating that the relative importance of electromagnetic effects is similar in the two cases.

The growth rate and the ratio of the electromagnetic and electrostatic field energy are calculated as shown in Fig. 4. In the left frame, the growth rate increases as n increases and reaches a saturation level, and then decreases. In the right frame, the field energy ratio E_A/E_{ϕ} quantifies the relative contribution of the electromagnetic field energy associated with δA_{\parallel} , where E_A and E_{ϕ} are the field energy associated with δA_{\parallel} and $\delta\phi$ as defined in the previous work [5]. For low n modes, the electromagnetic effect is more significant as shown by the higher value of E_A/E_{ϕ} . In both the growth rate and the energy ratio, the results of the instabilities in the core and near the separatrix are similar since the n and T profiles are similar near \tilde{r}_0 and the difference are mainly due to the contribution from other equilibrium parameters such as the local safety factor, the magnetic field strength at different minor-radius locations.

4.3 Electromagnetic simulations for various β

The relevance of the electromagnetic effects is evaluated by varying the value of the plasma β . As β increases, the dominant instability can change from the ITG mode to the KBM according to previous studies [27, 28, 29]. The β effect on the $n = 10$ harmonic of case 1a is shown in Fig. 5. It suggests that in the ITG mode transits to a KBM as β/β_{ref} changes from 0.2 to 2.0. The nominal $\beta = \beta_{\text{ref}}$ is close to the ITG-KBM transition threshold for $n = 10$. It should be noted that the KBM-ITG transition relies on multiple parameters such as β and n , thus for different parameters such as n , the critical β can be different. In the right frame, the field energy ratio increases with β , indicating stronger electromagnetic effects. For the nominal value of β , the field energy ratio shows that the electromagnetic field energy associated with δA_{\parallel} is significant, and the transport due to the electromagnetic effect should be verified.

4.4 Instability with different normalized machine size (a/ρ_{ref})

Simulations with smaller normalized machine size are carried out using cases 2a and 2b in Tab. 2. The growth rate and the energy ratio are shown in Fig. 6. Compared with the results for $\rho_{\text{ref}} = 0.3539 \text{ cm}$ (cases 1a and 1b) shown in Fig. 4, the $\gamma - n$ spectrum downshifts and thus the

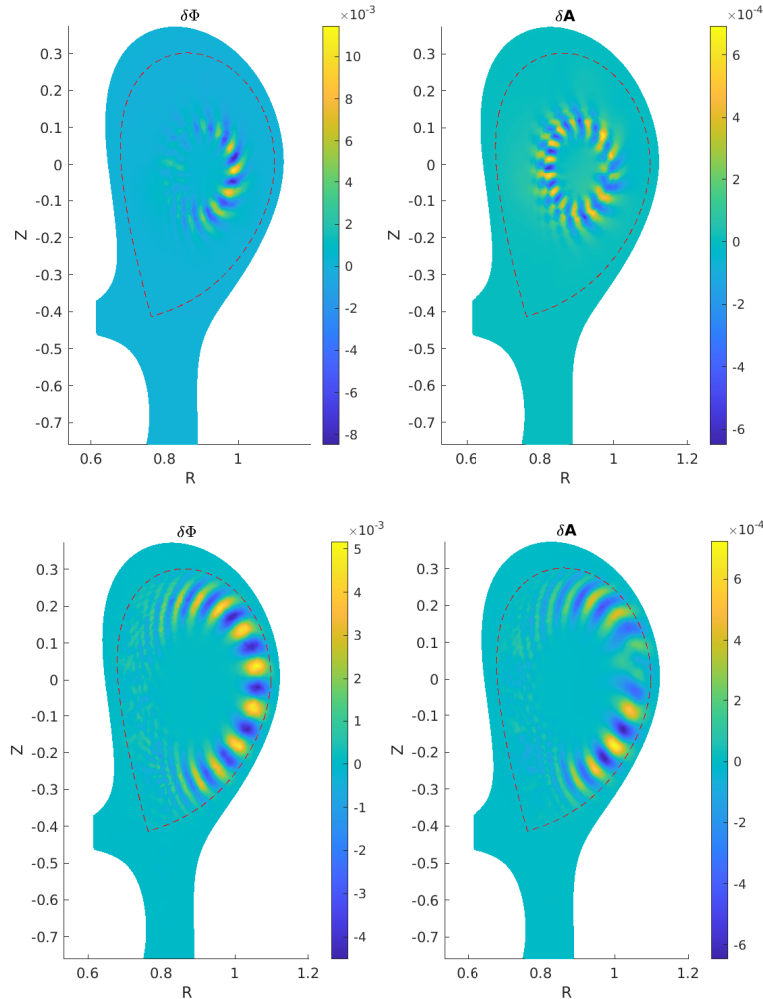


Figure 3. The 2D structures of $\delta\phi$ and δA_{\parallel} for the $n = 10$ ITG mode (Section 4.2). Top row: case 1a; bottom row: case 1b.

instability is dominated by modes with lower n . The energy ratio E_A/E_{ϕ} is smaller compared with Fig. 4. As ρ_{ref} increases, the energy ratio decreases, indicating a weaker electromagnetic effect, which agrees with the observation in the 1D model (Fig. 1 of [13]).

For numerical studies, higher ρ_{ref} brings in benefit since as ρ_{ref}/a increases, the marker number can be smaller and the time step size can be larger to achieve the same simulation quality, as observed previously in TRIMEG-C1 [5]. In the multi- n nonlinear simulations in Section 4.5, we will use $\rho_{\text{ref}} = 1$ cm.

4.5 Multi- n nonlinear simulations

Multi- n nonlinear simulations of case 2a and case 2b are performed using a piecewise field-aligned solver without toroidal filtering. The simulations cover the full toroidal domain, $\phi \in [0, 2\pi]$. In the simulation of the core/edge instability, $\{8, 8\} \times 10^6$ electron markers and $\{4, 2\} \times 10^6$ ion markers are simulated. The time step size was chosen as $\Delta t/t_N = \{0.005, 0.004\}$. Completing ~ 20000 steps on 4 nodes (1024 cores) of a cluster with AMD EPYC 9754 128-Core Processors (2 processors per node) took $\sim \{72, 60\}$ hours. The time evolution of the total field energy and the field energy ratio is demonstrated in Fig. 7. The instability growth rates γ_{AP} , γ_A , γ_P are calculated from the total field energy $E_{\text{tot}} = E_{\phi} + E_A$, E_A and E_{ϕ} , respectively. These energies are assumed to evolve as $E_{[\text{tot}, A, \phi]} = E_{[\text{tot}, A, \phi]}(t=0) \exp\{2\gamma_{[AP, A, P]}t\}$ at linear stage. The growth rates are measured during the linear stage $25 < t/t_N < 35$ for case 2a and $15 < t/t_N < 25$ for case 2b. As shown in the right frame of Fig. 7, the instability is dominated by the electrostatic component since the electromagnetic energy ratio is relatively low with $E_A/E_{\text{tot}} < 0.15$.

The most unstable mode appears and becomes dominant in the late linear stage ($t/t_N \in [25, 35]$ for case 2a and $t/t_N \in [15, 25]$ for case 2b), and the 2D mode structure is shown in Fig. 8. The growth rate and the field energy ratio measured during the linear stage are also plotted in Fig. 6

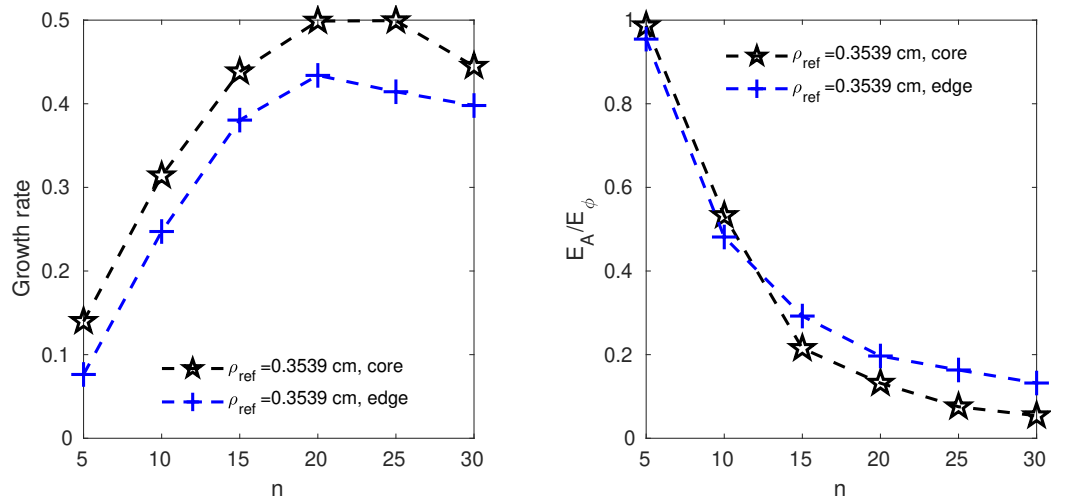


Figure 4. The growth rate (left) and the ratio of the field energy (right) across the spectrum of toroidal mode number n for instabilities in the core (case 1a) and near the separatrix (case 1b) (Section 4.2).

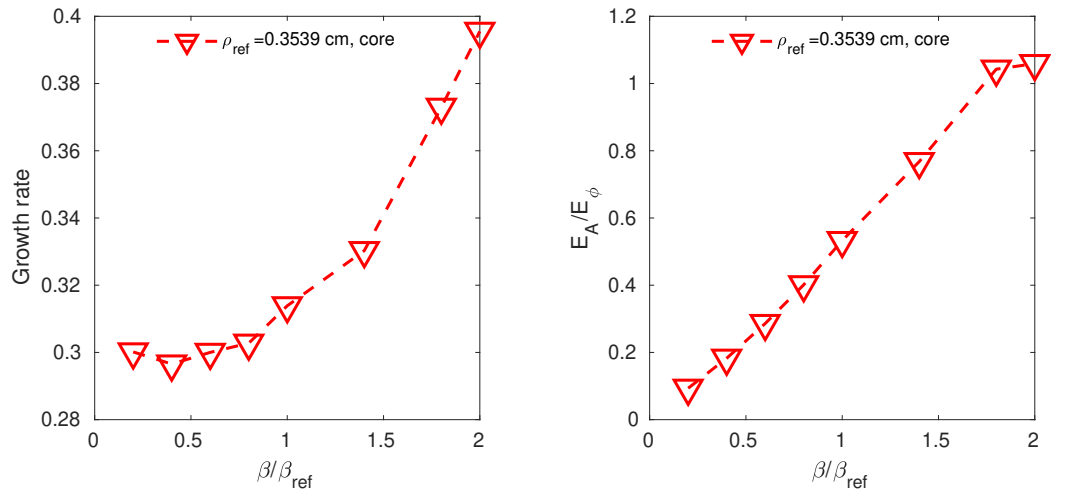


Figure 5. The growth rate (left) and the ratio of the field energy (right) for different values of β_{ref} (β scan based on case 1a) for the $n = 10$ harmonic. (Section 4.3).

for comparison with the single- n simulation, which are indicated by the blue and black transparent bars. The dominant mode numbers $n \sim 6 - 10$ for case 2a and $n \sim 7 - 11$ for case 2b in the multi- n simulations are indicated by the widths of the bars. The growth rate and the energy ratio are similar to those of the most unstable mode from the single- n simulations, while the minor difference is due to the finite error of the measurement.

5 Conclusions

In this work, a high-order C^1 -continuous piecewise field-aligned finite element method on unstructured triangular meshes has been extended and implemented in the TRIMEG-C1 gyrokinetic particle-in-cell framework for whole-volume electromagnetic simulations of tokamak plasmas with open field lines. By combining C^1 triangular finite elements, mixed-variable formulations, and a generalized pullback scheme, the developed approach enables efficient and stable simulations of electromagnetic micro instabilities in complex geometries spanning the core, separatrix, and open field line regions.

The piecewise field-aligned finite element method formulated in cylindrical coordinates significantly reduces grid distortion associated with magnetic shear while retaining field-line alignment locally within each toroidal subdomain. This feature proves essential for whole-volume simulations, where global field-aligned coordinates become impractical. The formulation is fully compatible with both δf and full- f models and supports the iterative solution of Ampère's law with analytically well-controlled skin-depth terms, ensuring robust convergence in electromagnetic regimes.

Linear simulations of the TCV-X21 configuration demonstrate that the developed scheme accurately captures electromagnetic ion-temperature-gradient and kinetic ballooning mode physics. Systematic parameter scans in toroidal mode number, plasma β , and normalized machine size con-

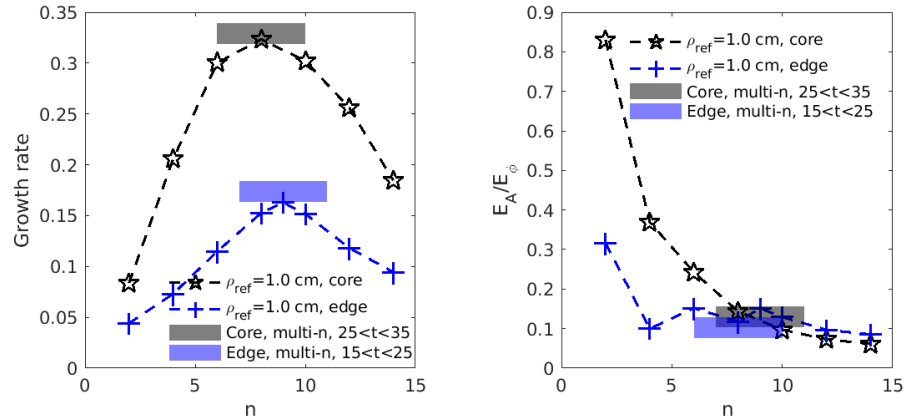


Figure 6. The growth rate (left) and the ratio of the field energy (right) across the toroidal mode spectrum with $\rho_{\text{ref}} = 1 \text{ cm}$ for core (case 2a) and edge (case 2b) instabilities (Section 4.4). The growth rate and the ratio of the field energy during the linear stage in multi- n simulations are indicated by the wide black and blue transparent bars (Section 4.5).

firm expected physical trends, including the ITG–KBM transition and the downshift of the dominant instability spectrum at reduced a/ρ_{ref} . Multi- n nonlinear simulations further validate the capability of the piecewise field-aligned solver to handle fully three-dimensional electromagnetic turbulence without toroidal filtering.

Overall, the results establish TRIMEG-C1 with the present high-order piecewise field-aligned finite element method as a powerful and flexible tool for global electromagnetic gyrokinetic simulations in realistic tokamak geometries with open field lines. Future work will focus on incorporating finite Larmor radius effects, extending the approach to fully nonlinear electromagnetic turbulence in the edge and scrape-off layer, and performing quantitative validation against experimental measurements.

Acknowledgments

The discussion with A. Stegmeir and Ph. Ulbl on the TCV case and the discussion with M. Borchardt are appreciated. The simulations in this work were run on the local TOK cluster and the MPCDF Viper/Raven supercomputers. The EUROfusion projects TSVV-8, ACH/MPG, TSVV-10, TSVV-G, and ATEP are acknowledged. This work has been carried out within the framework of the EUROfusion Consortium, funded by the European Union via the Euratom Research and Training Programme (Grant Agreement No 101052200—EUROfusion). Views and opinions expressed are however those of the author(s) only and do not necessarily reflect those of the European Union or the European Commission. Neither the European Union nor the European Commission can be held responsible for them.

References

- [1] Mishchenko A, Biancalani A, Borchardt M, Bottino A, Briguglio S, Dumont R, Ferreira J, Graves J, Hayward-Schneider T, Kleiber R *et al.* 2023 *Plasma Physics and Controlled Fusion* **65** 064001
- [2] Lanti E, Ohana N, Tronko N, Hayward-Schneider T, Bottino A, McMillan B F, Mishchenko A, Scheinberg A, Biancalani A, Angelino P *et al.* 2020 *Computer Physics Communications* **251**
- [3] Taimourzadeh S, Bass E, Chen Y, Collins C, Gorelenkov N, Könies A, Lu Z, Spong D A, Todo Y, Austin M *et al.* 2019 *Nuclear Fusion* **59** 066006
- [4] Chang C, Ku S, Tynan G, Hager R, Churchill R, Cziegler I, Greenwald M, Hubbard A and Hughes J 2017 *Phys. Rev. Lett.* **118** 175001
- [5] Lu Z X, Meng G, Hatzky R, Sonnendrücker E, Mishchenko A, Lauber P, Zonca F and Hoelzl M 2024 *Plasma Physics and Controlled Fusion* **67** 015015
- [6] Lu Z X, Meng G, Sonnendrücker E, Hatzky R, Mishchenko A, Zonca F, Lauber P and Hoelzl M 2025 *Journal of Plasma Physics* **91** E48

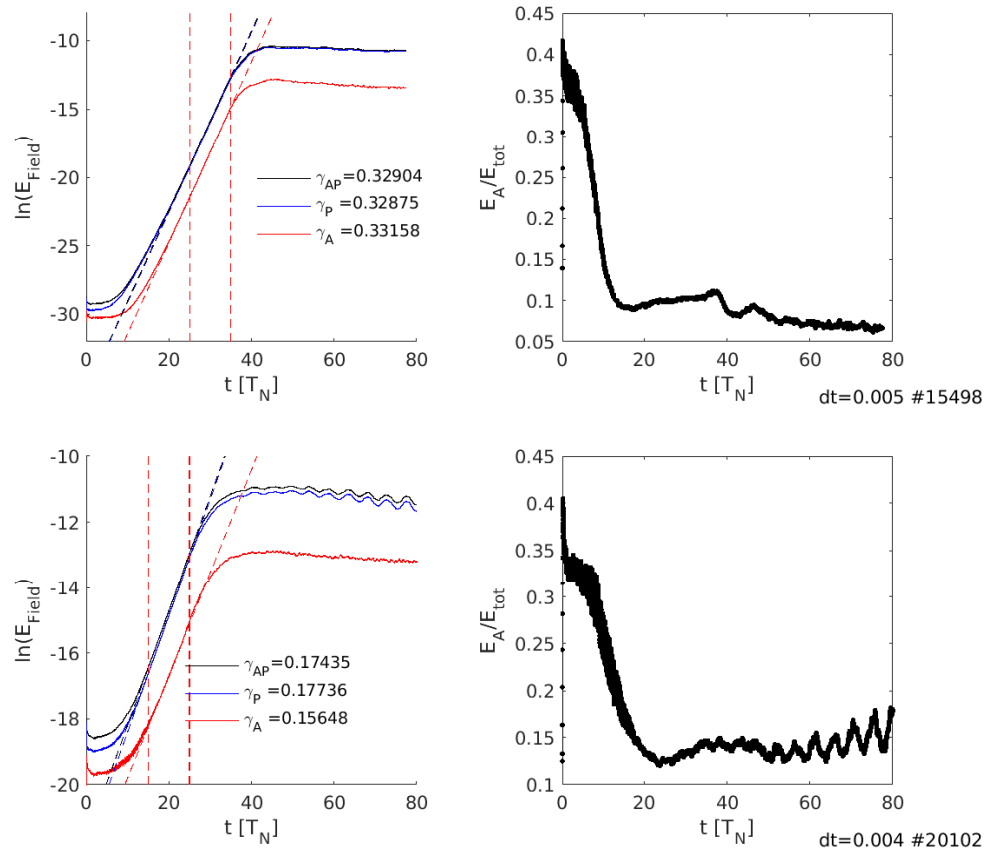


Figure 7. The time evolution of the total field energy (left) and the field energy ratio (right) for the core instability (upper frame) and the edge instability (lower frame) in the nonlinear multi-harmonic simulations (Section 4.5).

- [7] Lu Z X, Meng G, Hatzky R, Lauber P and Hoelzl M 2026 *Computer Physics Communications* **320** 109959 ISSN 0010-4655 URL <https://www.sciencedirect.com/science/article/pii/S0010465525004606>
- [8] Hariri F and Ottaviani M 2013 *Computer Physics Communications* **184** 2419–2429
- [9] Stegmeir A, Coster D, Ross A, Maj O, Lackner K and Poli E 2018 *Plasma Physics and Controlled Fusion* **60** 035005
- [10] Scott B D 2001 *Physics of Plasmas* **8** 447–458
- [11] Mishchenko A, Könies A, Kleiber R and Cole M 2014 *Physics of Plasmas* **21**
- [12] Hatzky R, Kleiber R, Könies A, Mishchenko A, Borchardt M, Bottino A and Sonnendrücker E 2019 *Journal of Plasma Physics* **85**
- [13] Lu Z X, Meng G, Hatzky R, Sonnendrücker E, Mishchenko A and Hoelzl M 2025 *Physics of Plasmas* **32** 122112 ISSN 1070-664X URL <https://doi.org/10.1063/5.0303674>
- [14] Moritaka T, Hager R, Cole M, Lazerson S, Chang C S, Ku S H, Matsuoka S, Satake S and Ishiguro S 2019 *Plasma* **2** 179–200
- [15] Mishchenko A, Borchardt M, Hatzky R, Kleiber R, Könies A, Nührenberg C, Xanthopoulos P, Roberg-Clark G and Plunk G G 2023 *Journal of Plasma Physics* **89** 955890304
- [16] Kleiber R, Borchardt M, Hatzky R, Könies A, Leyh H, Mishchenko A, Riemann J, Slaby C, García-Regaña J, Sanchez E *et al.* 2024 *Computer Physics Communications* **295** 109013
- [17] Lu Z X, Meng G, Hatzky R, Hoelzl M and Lauber P 2023 *Plasma Physics and Controlled Fusion*
- [18] Chen Y and Parker S E 2007 *Journal of Computational Physics* **220** 839–855

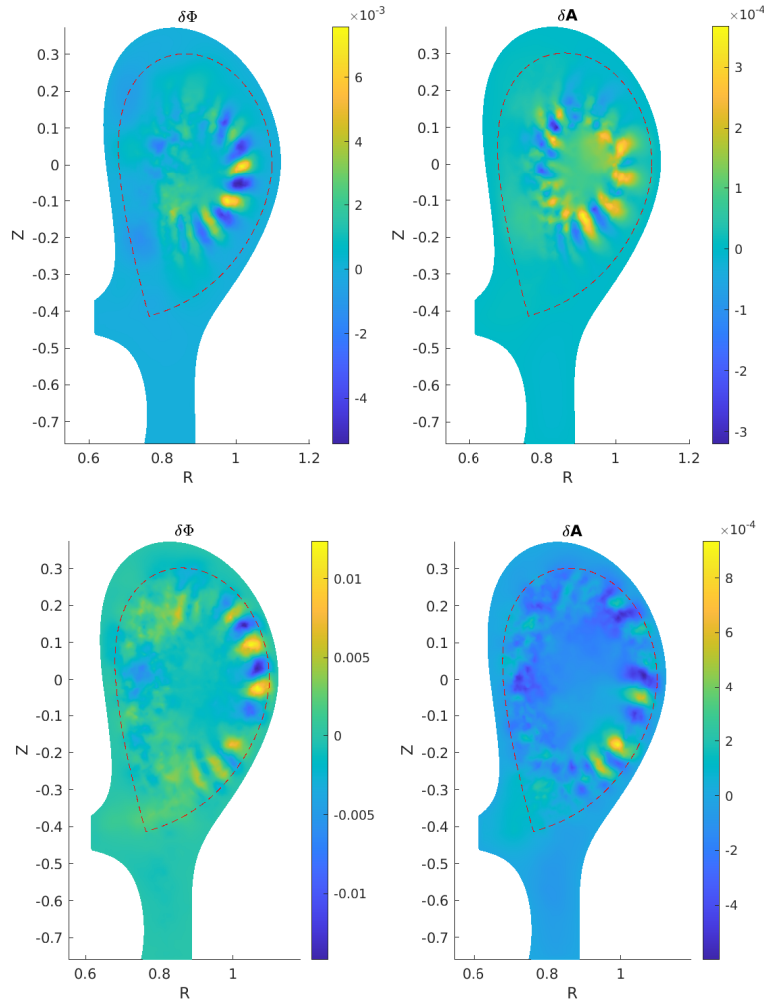


Figure 8. The 2D mode structures of the core instability ($t/t_N = 35$, upper frame) and the edge instability ($t/t_N = 30$, lower frame) at the late linear stage of multi- n nonlinear simulations (Section 4.5).

- [19] Mishchenko A, Bottino A, Hatzky R, Sonnendrücker E, Kleiber R and Könies A 2017 *Physics of Plasmas* **24**
- [20] McMillan B F 2017 *Computer Physics Communications* **212** 39–46
- [21] Oliveira D, Body T, Galassi D, Theiler C, Laribi E, Tamain P, Stegmeir A, Giacomin M, Zholobenko W, Ricci P *et al.* 2022 *Nuclear Fusion* **62** 096001
- [22] Body T A J 2022 *Development of Turbulence Simulations for the Edge & Divertor and Validation against Experiment* Ph.D. thesis Technische Universität München
- [23] Ulbl P, Body T, Zholobenko W, Stegmeir A, Pfennig J and Jenko F 2023 *Physics of Plasmas* **30**
- [24] Chen L and Zonca F 2016 *Reviews of Modern Physics* **88** 015008
- [25] Zonca F and Chen L 2014 *Physics of Plasmas* **21**
- [26] Lu Z X, Zonca F and Cardinali A 2012 *Physics of Plasmas* **19**
- [27] Zonca F, Chen L, Dong J and Santoro R A 1999 *Physics of Plasmas* **6** 1917–1924
- [28] Aleynikova K and Zocco A 2017 *Physics of Plasmas* **24**
- [29] Görler T, Tronko N, Hornsby W A, Bottino A, Kleiber R, Norscini C, Grandgirard V, Jenko F and Sonnendrücker E 2016 *Phys. Plasmas* **23**